Journal of Sound and Vibration (1998) **209**(1), 77–97

PRECONDITIONING THE HELMHOLTZ EQUATION

K. J. BAUMEISTER

KJB Consultants, 7380 *Baldwin Creek Drive*, *Middleburg Hts*, *OH* 44130-5544, *U.S.A.*

AND

K. L. KREIDER

Department of Mathematical Sciences, *The University of Akron*, *Akron*, *OH* 44325-4002, *U.S.A.*

(*Received* 24 *January* 1997, *and in final form* 24 *July* 1997)

An innovative hyperbolic preconditioning technique is developed for the numerical solution of the Helmholtz equation which governs acoustic propagation in ducts. Two pseudo-time parameters are used to produce an explicit iterative finite difference scheme. This scheme eliminates the large matrix storage requirements normally associated with numerical solutions to the Helmholtz equation. The solution procedure is very fast. It is one order of magnitude faster than a previously developed parabolic preconditioning approach. Optimization and an error analysis of the preconditioning factors are present. For validation, the method is applied to sound propagation in a 2-D semi-infinite hard wall duct and a soft-walled sound absorbing duct.

1. INTRODUCTION

The Helmholtz equation plays an important role in the study of acoustics as well as electromagnetic propagation and quantum mechanics. Unfortunately, large matrix storage requirements are generally associated with numerical solutions of the Holmholtz equation. To reduce these requirements, Bayless *et al*. [1] developed an iterative approach to solve the associated matrix equation. More recently, Baumeister and Kreider [2] developed a preconditioned transient finite difference scheme to solve the Helmholtz equation as well as the more general linearized potential flow equations. Their introduction of time dependence into the Helmholtz equation eliminates the large matrix storage requirements of the algorithm. This paper is concerned with the development of a more efficient preconditioning method to accelerate convergence for the Helmholtz equation.

A standard technique of solving steady-state partial differential equations is to march their time dependent form until the steady-state is reached. When the transient is not of interest, acceleration parameters can be employed to speed the convergence. This type of differential manipulation is often associated with preconditioning of both time dependent and time independent [3] partial differential equations. Generally, acceleration parameters destroy the time accuracy of the solution.

New hyperbolic preconditioning factors are introduced to speed the convergence of the transient finite difference scheme in solving the Helmholtz equation. Solution times are reduced by an order of magnitude over the previous parabolic preconditioning approach. For validation, the method is applied to plane wave sound propagation in a 2-D

0022–460X/98/010077 + 21 $25.00/0/sv971235

semi-infinite hard wall duct and a short soft-walled sound absorbing duct. The paper contains a description of the problem, the brief development of the preconditioning technique, the introduction of the acceleration parameters, the finite difference formulation with a stability analysis, and several numerical examples with error estimates.

2. PROBLEM STATEMENT

The problem under consideration here is the development of preconditioning acceleration factors to obtain the solution to the Helmholtz equation. This method will have application to the general study of sound propagation in ducts. The goal is to develop a stable, explicit finite difference scheme that significantly reduces the computation time required to solve the Helmholtz equation with a monochromatic noise source. The formulation is applied to a semi-infinite duct with a planar source at the duct inlet, as shown in Figure 1.

3. HELMHOLTZ EQUATION AND BOUNDARY CONDITION

The governing differential equation for studying wave propagation can be formulated in terms of a potential as

$$\frac{1}{C^2}\phi'_{tt} = \phi'_{xx} + \phi'_{yy} \qquad \text{or} \qquad f^2\phi'_{tt} = \phi'_{xx} + \phi'_{yy}, \tag{1}$$

where $\phi'(x, y, t)$ is the dimensionless potential and subscripts indicate partial differentiation with respect to subscripted variables. The conventional normalization factors used to develop these non-dimensional equations are in a list of nomenclature given in the Appendix. The dimensionless frequency f is defined as

$$f = \frac{f^{\#}D^{\#}}{C_o^{\#}} = \frac{1}{C}, \tag{2}$$

where the superscript $\#$ indicates a dimensional quantity.

There are several ways to develop a frequency domain formulation for equation (1). The Fourier Transform can be applied if the potential has a multi-frequency content. In the monochromatic case, this is equivalent to assuming that

$$\phi'(x, y, t) = \psi(x, y)\, \mathrm{e}^{-i\omega^{\#}t^{\#}} = \psi(x, y)\, \mathrm{e}^{-i2\pi t} \tag{3}$$

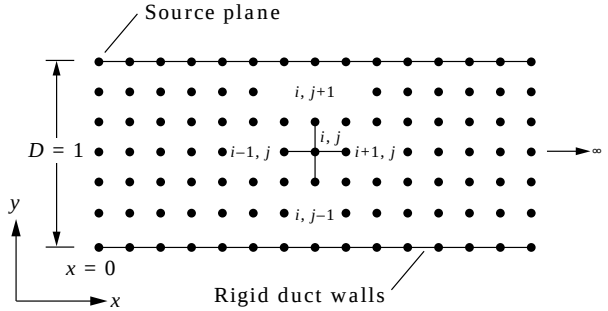

Figure 1. Structured finite difference-time dependent (FD-TD) mesh for semi-infinite rectangular duct.

which transforms equation (1) to the Helmholtz equation

$$0 = \psi_{xx} + \psi_{yy} + \omega^2\psi, \tag{4}$$

where $\omega = 2\pi f$.

At the entrance of the duct, $x = 0$, the source is assumed to have the form

$$\phi' = \mathrm{e}^{-i2\pi t} \qquad \text{or} \qquad \Psi = 1. \tag{5}$$

Also, the duct is assumed to be semi-infinite in length so that waves propagate only to the right.

4. PRECONDITIONED HELMHOLTZ EQUATION

The Helmholtz equation is preconditioned by assuming that

$$\phi'(x, y, t) = \phi(x, y, t)\,\mathrm{e}^{-i\omega^{\#}t^{\#}} = \phi(x, y, t)\,\mathrm{e}^{-i2\pi t}. \tag{6}$$

See reference [2] for further discussion. This differs from the classical monochromatic transformation in that the amplitude ϕ (no prime) is no longer independent of time. Under this transformation, equation (1) becomes

$$f^2\phi_{tt} - 2if\omega\phi_t = \phi_{xx} + \phi_{yy} + \omega^2\phi. \tag{7}$$

The only difference between the Helmholtz equation (4) and equation (7) is the presence of the time derivative terms on the left hand side. Physically, the time dependence in $\phi(x, y, t)$ is caused by assuming that the duct is quiescent at time 0, and that the source is turned on at that instant. A series of numerical calculations reported by Baumeister and Kreider [2] show that

$$\lim_{t\to\infty} \phi(x, y, t) = \psi(x, y) \tag{8}$$

when the $f^2\phi_{tt}$ is dropped (parabolic approximation).

5. ACCELERATION PARAMETERS

To speed the convergence to the steady-state solution $\psi(x, y)$, acceleration parameters α and β are added to equation (7) as follows:

$$\alpha f^2\phi_{tt} - \beta 2if\omega\phi_t = \phi_{xx} + \phi_{yy} + \omega^2\phi. \tag{9}$$

This is a generalization of the preconditioning done in reference [2], which dealt with the $\alpha = 0$, $\beta = 1$ case, herein denoted the parabolic preconditioner because the second-order time derivative does not appear. After the formulation of the difference equations, the acceleration of convergence is tested over a range of acceleration parameters.

6. FINITE DIFFERENCE EQUATIONS

The potential at the spatial grid points (x_i, y_j) (Figure 1) is determined by iterating the initial condition over time steps $t^k = k\,\Delta t$. Away from the duct boundaries, each partial

derivative in equation (9) can be expressed using central differences, which yields

$$\phi_{i,j}^{k+1}\left(\frac{\alpha f^2}{\Delta t^2}-\frac{-\beta i\omega f}{\Delta t}\right)=\phi_{i,j}^{k}\left(\frac{2\alpha f^2}{\Delta t^2}-\frac{2}{\Delta x^2}-\frac{2}{\Delta y^2}+\omega^2\right)$$
$$+\phi_{i+1,j}^{k}\left(\frac{1}{\Delta x^2}\right)+\phi_{i-1,j}^{k}\left(\frac{1}{\Delta x^2}\right)$$
$$+\phi_{i,j+1}^{k}\left(\frac{1}{\Delta y^2}\right)+\phi_{i,j-1}^{k}\left(\frac{1}{\Delta y^2}\right)$$
$$+\phi_{i,j}^{k-1}\left(-\frac{\alpha f^2}{\Delta t^2}-\frac{\beta i\omega f}{\Delta t}\right), \tag{10}$$

where Δx, Δy and Δt are the space and time mesh spacings respectively, and $\phi_{ij}^{k}=\phi(x_i, y_j, t^k)$. Equation (10) is an explicit two-step scheme. The field values at t^0 and t^{-1} are assumed to be zero because the initial field is quiescent.

The expressions for the difference equations at the hard wall boundaries ($y=0$ and $y=1$) employ the boundary condition

$$\nabla\phi\cdot n=0, \tag{11}$$

where n is the unit outward normal. Baumeister [4] gives precise details for generating the difference equations on the boundaries.

7. STABILITY

A von Neumann stability analysis is used to determine the conditions on Δt, Δx and Δy required for conditional stability as a function of the acceleration parameters α and β. Conditional stability means that the amplification factor, which describes how errors propagate from one time step to the next, has magnitude one. Thus, when Δt, Δx and Δy satisfy the stability criteria, errors are not magnified or diminished in magnitude. This is a desirable property, since the numerical formulation cannot distinguish between a roundoff error and a small physical oscillation.

For the parabolic preconditioner ($\alpha=0$, $\beta=1$), the stability analysis [2] indicates that the method is conditionally stable, subject to the condition

$$\Delta t<\frac{1}{(2/\omega f)[(1/\Delta x)^2+(1/\Delta y)^2]-\pi+|M|/f\,\Delta x}. \tag{12}$$

In a typical application, f is set by the operating conditions in the duct. The grid spacing parameters Δx and Δy are set to resolve the estimated spatial harmonic variation of the potential field and Δt is chosen to satisfy equation (12). Of course, the stability analysis does not take into account boundary conditions. For stability, gradient boundary conditions generally require the use of smaller Δt than predicted by equation (12).

For the case $\alpha\neq 0$ and $\beta\neq 0$, herein denoted the mixed preconditioner, the stability analysis indicates that the method is conditionally stable, subject to the two conditions

$$\Delta t<\frac{1}{\pi}\sqrt{(\beta^2-\alpha)} \tag{13}$$

and

$$\Delta t < \sqrt{\frac{\alpha f^2}{1/\Delta x^2 + 1/\Delta y^2 - \omega^2/4} + \left(\frac{\beta\pi f^2}{1/\Delta x^2 + 1/\Delta y^2 - \omega^2/4}\right)^2}. \tag{14}$$

Equation (13) implies that $\beta^2 > \alpha$ and that a hyperbolic formulation without the first time derivative ($\beta = 0$) would be unstable. Generally, the second squared term on the right side of equation (14) is much smaller than the first term. For a typical scenario ($\Delta x = 0{\cdot}05$, $\Delta y = 0{\cdot}1$, $f = 1$, $\alpha = 0{\cdot}95$, $\beta = 1$), $\Delta t < 0{\cdot}071$ from equation (13) and $\Delta t < 0{\cdot}044$ from equation (14). Consequently, the stability criteria yield $\Delta t < 0{\cdot}044$ in this mixed case example.

8. NUMERICAL EXAMPLES

Let a plane wave propagate from the left into a semi-infinite quiescent duct. The potential field is to be computed in the duct for $0 < x < 1$. Examples (1)–(3) illustrate the effects of changing α and β with dimensionless frequency $f = 1$ on the grid specified by $\Delta x = 0{\cdot}05$ and $\Delta y = 0{\cdot}5$. Example 4 shows the effect of increasing the frequency, by using $f = 5$.

Because boundary conditions can introduce instabilities [5, 6] into otherwise stable finite difference schemes, it is important to test the iteration scheme for convergence in the absence of an exit boundary condition. Therefore, in these examples, the computational boundary is set at $x = 50$, far enough away from the true boundary $x = 1$ that any artifacts arising from the exit boundary condition do not affect the solution in $0 < x < 1$.

The numerical results for plane wave propagation are compared to the exact results of the steady-state solution, given by

$$\psi(x) = \mathrm{e}^{i\omega x}. \tag{15}$$

In the region $0 < x < 1$, the L_1 norm of the global error e_k between the exact solution ψ and the numerical solution ϕ^k at time step k is used as a measure of the convergence. The error is defined as

$$e_k = \int_0^1 \int_0^1 \sqrt{(\phi^k - \psi)\overline{(\phi^k - \psi)}}\, \mathrm{d}y\, \mathrm{d}x. \tag{16}$$

8.1. EXAMPLE 1: PARABOLIC PRECONDITIONING ($\alpha = 0$, $\beta = 1$, $f = 1$)

The choice of $\alpha = 0$ eliminates the second order time derivative. The time increment Δt is set at 0·007. The maximum stable value, from equation (12), is 0·00797. The numerical and exact solutions are compared in Figure 2(a) (real and imaginary parts of the potential) and in Figure 2(b) (magnitude of the potential) after 1000 iterations. The numerical solution shows excellent agreement with the analytic solution. The error as a function of the iteration number is shown in Figure 3. After 1000 iterations, $e_{1000} = 0{\cdot}0171$. This residual error is the result of the usual round-off and truncation errors associated with finite differences.

8.2. EXAMPLE 2: MIXED PRECONDITIONING ($\alpha = 0{\cdot}95$, $\beta = 1$, $f = 1$)

The time increment Δt is set at 0·04. The maximum stable value, from equation (14), is 0·049. The error as a function of the iteration number is shown in Figure 4. After 100 iterations, $e_{100} = 0{\cdot}0136201$. It is important to note that the number of iterations required

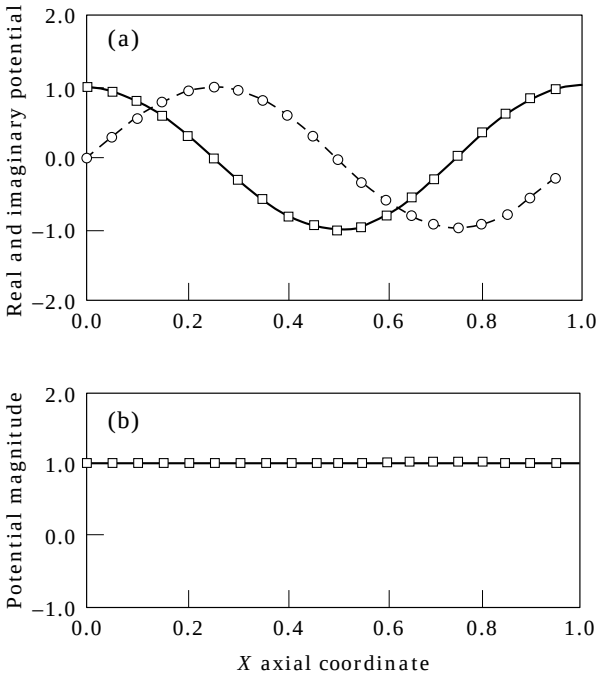

Figure 2. Analytical and numerical profile along wall for plane propagation in a semi-infinite hard walled duct ($f = 1$). (a) Real and imaginary parts with $\alpha = 0$ and $\beta = 1{\cdot}0$. Numerical solution: □, real potential; ○, imaginary potential. Exact analytical solution: ——, real potential; – – –, imaginary potential. (b) Magnitude with $\alpha = 0$ and $\beta = 1{\cdot}0$. Numerical solution: □, magnitude potential. Exact analytical solution: ——, magnitude.

for convergence drops by an order of magnitude with mixed preconditioning as compared to parabolic preconditioning (shown by dashed line in Figure 4). Therefore, a calculation which took 1 min with the parabolic approach would now take only 6 s with the hyperbolic approach. Again, the numerical solution shows excellent agreement with the analytic solution after 100 iterations. The plots of the magnitude and the real and imaginary parts of the potential are virtually identical to Figures 2(a) and (b), and hence are omitted. Clearly, mixed preconditioning is superior to parabolic preconditioning because the number of iterations required for convergence is an order of magnitude lower.

8.3. EXAMPLE 3: MIXED PRECONDITIONING ($\alpha = 16$, $\beta = 4{\cdot}25$, $f = 1$)

The time increment Δt is set at 0·2. The maximum stable value, from equation (14), is 0·201. The error as a function of the number of iterations is shown in Figure 5. After 100 iterations, $e_{100} = 0{\cdot}0136225$. The results here are nearly identical to those shown in Figure 4. The numerical solution again shows excellent agreement with the analytic solution. As before, the plots of magnitude and phase are omitted because they are virtually identical to Figures 2(a) and (b). In this example, with the introduction of the large acceleration parameters, the time variable loses its physical meaning. In effect, the large α reduces the effective speed of propagation C in equation (1) which then requires a longer time for the transient ϕ to approximate the steady state solution ψ as required by equation (8). However, the critical parameter is the number of iterations required to obtain a solution. The convergence rates for examples (2) and (3) are nearly identical.

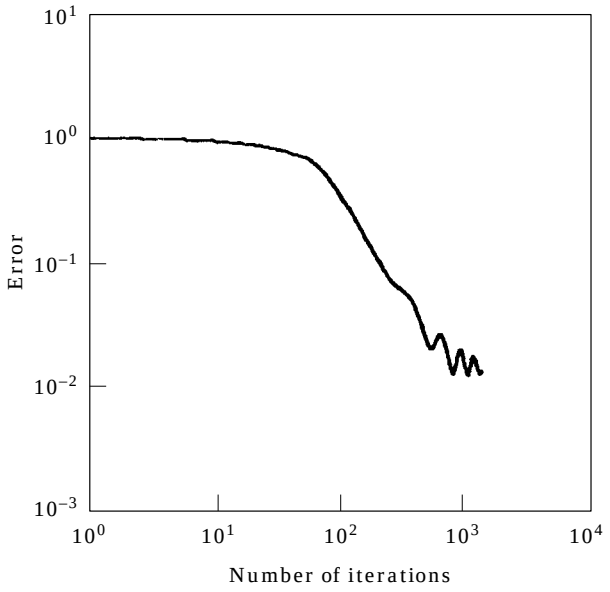

Figure 3. Integrated solution error as a function of the number of iterations of the finite difference equations ($f = 1$); parabolic approximation $\alpha = 0$ and $\beta = 1$.

8.4. EXAMPLE 4: MIXED PRECONDITIONING ($\alpha = 0{\cdot}95$, $\beta = 1$, $f = 5$)

To resolve the shorter wavelengths associated with the higher frequency $f = 5$, Δx is reduced by a factor of 5 to 0·01. The time increment Δt is set at 0·04. The maximum stable value, from equation (14), is 0·049. The incremental and exact solutions are compared in Figure 6(a) (real and imaginary parts of the potential) and in Figure 6(b) (magnitude of the potential) after 1000 iterations. The numerical solution again shows excellent

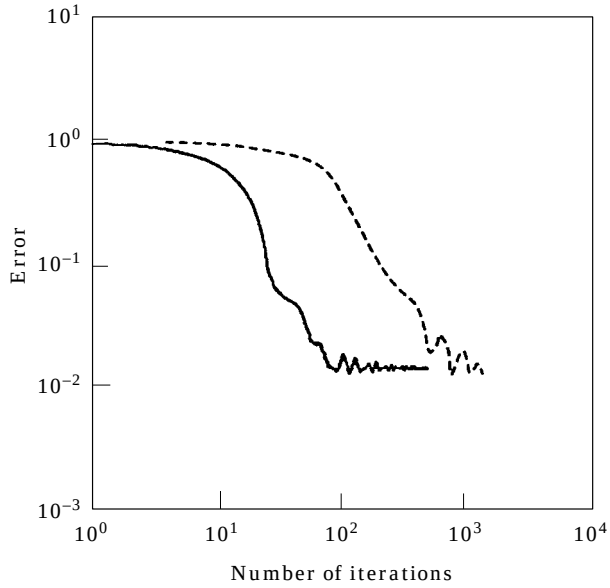

Figure 4. Integrated solution error as a function of the number of iterations of the finite difference equations ($f = 1$): – – –, parabolic $\alpha = 0$ and $\beta = 1{\cdot}0$; ——, mixed $\alpha = 0{\cdot}95$ and $\beta = 1{\cdot}0$.

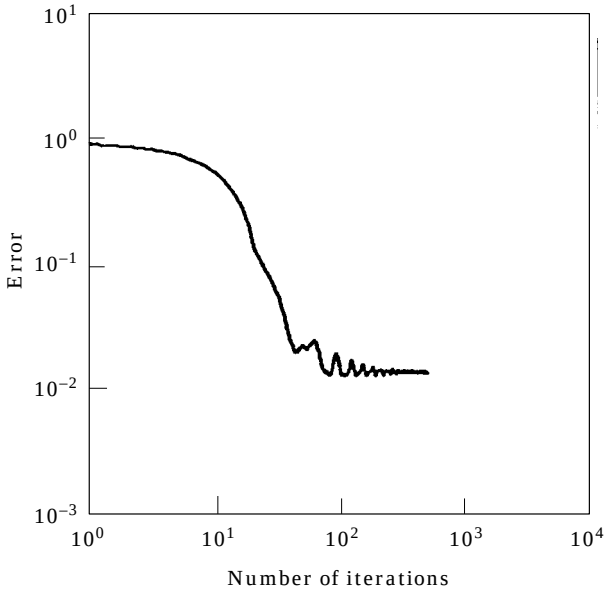

Figure 5. Integrated solution error as a function of the number of iterations of the finite difference equations ($f = 1$); mixed $\alpha = 16$ and $\beta = 4{\cdot}25$.

agreement with the analytic solution. The error as a function of iteration number is shown in Figure 7. After 1000 iterations, $e_{1000} = 0{\cdot}0659$. This error is about 5 times higher than that for the $f = 1$ case. Since the two solution plots show roughly the same degree of accuracy, the change in total global error is apparently caused by the fact that there are 5 times as many grid points in the $f = 5$ case. The number of grid points is proportional to the number of axial wavelengths or frequency. So dividing by the frequency gives a rough measure of the local error at each grid point, which is, in this case,

$$e_{k\lambda} = \frac{e_k}{f} = 0{\cdot}0132. \tag{17}$$

It should also be noted that acceptable solutions can be obtained using fewer iterations than the asymptotic values indicated by Figures 7–9.

9. OPTIMAL ACCELERATION PARAMETERS

Numerous numerical calculations were performed to determine the optimal choice of α and β to reduce the number of iterations to convergence. In these calculations α was set to 1 and β varied. Other choices of α yield approximately the same rate of convergence. For convergence with minimum iterations, the time increment Δt and β were set as follows:

$$\Delta t_{opt} = \sqrt{\frac{\alpha f^2}{\dfrac{1}{\Delta x^2} + \dfrac{1}{\Delta y^2} - \dfrac{\omega^2}{4}}}, \qquad \beta_{opt} = \sqrt{\alpha + \pi^2 \, \Delta t_{opt}^2}. \tag{18, 19}$$

For $\alpha = 1$, $\Delta x = 0{\cdot}05$, $\Delta y = 0{\cdot}5$ and $f = 1$, the optimal time increment Δt_{opt}, from equation (18), is 0·0503. The optimal β_{opt} is calculated to be 1·01244 from equation (19). The error as a function of the number of iterations is shown in Figure 8. After 100

iterations, $e_{100} = 0{\cdot}0137$. The converged error is nearly identical to the $\alpha = 0{\cdot}95$ and $\beta = 1{\cdot}0$ non-optimal case shown in Figure 4. However, the optimal case reaches this error with nearly one order of magnitude in fewer iterations. Also, the error curve is seen to be much smoother. Therefore, a calculation which took 1 min with the parabolic approach would now take only 1·8 s with the hyperbolic approach. The numerical solution again shows excellent agreement with the analytic solution. As before, the plots of magnitude and phase are omitted because they are virtually identical to Figures 2(a) and (b).

The number of iterations to obtain the final solution can be reduced even further by increasing the spatial distance between nodes. For $\alpha = 1$, $\Delta x = 0{\cdot}0833$ (66% increase), $\Delta y = 0{\cdot}5$ and $f = 1$, the optimal time increment Δt_{opt} from equation (18) is 0·0851. The optimal β_{opt} is calculated to be 1·03614 from equation (19) with a 1·001 factor of safety. The error as a function of the number of iterations is shown in Figure 9. After 100 iterations, $e_{100} = 0{\cdot}0398$, which is approximately 3 times larger than the previous case shown in Figure 8 with $\Delta x = 0{\cdot}05$. However, this error is still acceptable for accurate solutions. In fact, after 16 iterations, the error level has dropped to 0·04732, which gives excellent results for phase and magnitude plots of the potential as shown in Figures 10(a) and (b).

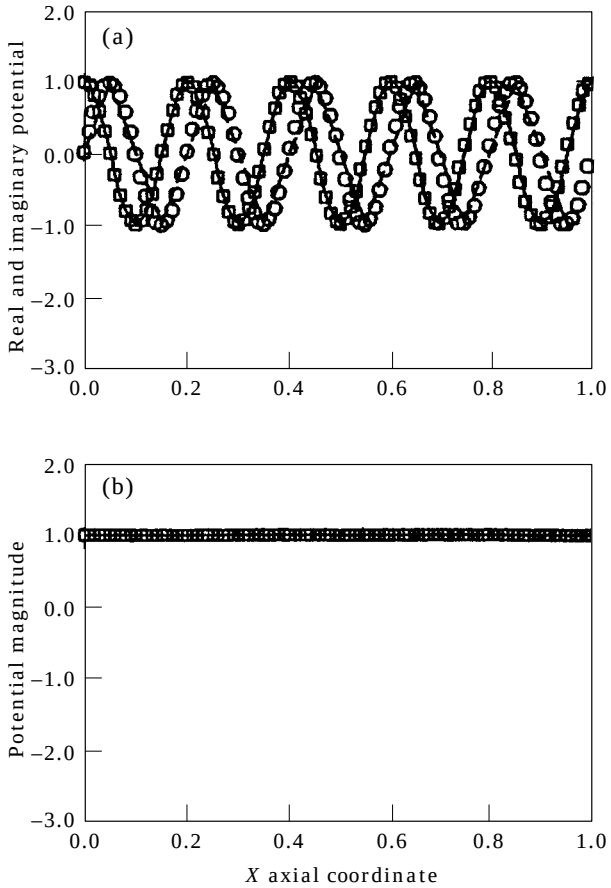

Figure 6. Analytical and numerical potential profile along wall for plane wave propagation in a semi-finite hard walled duct ($f = 5$). (a) Real and imaginary parts with $\alpha = 0{\cdot}95$ and $\beta = 1{\cdot}0$. Numerical solution: □, real potential; ○, imaginary potential. Exact analytical solution: ——, real potential; – – –, imaginary potential. (b) Magnitude with $\alpha = 0{\cdot}95$ and $\beta = 1{\cdot}0$. Numerical solution: □, magnitude potential. Exact analytical solution: ——, magnitude.

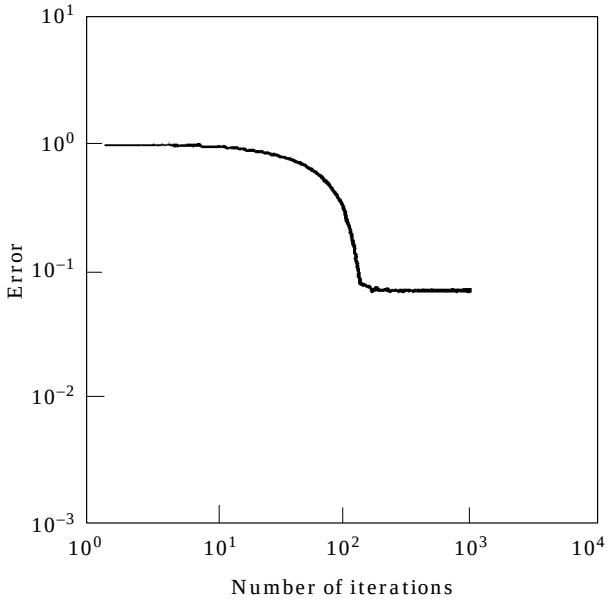

Figure 7. Integrated solution error as a function of the number of iterations of the finite difference equations ($f = 5$); mixed $\alpha = 0{\cdot}95$ and $\beta = 1{\cdot}0$.

The error for a wide range of grid spacing is shown in Figure 11. The error decreases for smaller Δx; however, the number of iterations to obtain the smaller asymptotic error becomes large.

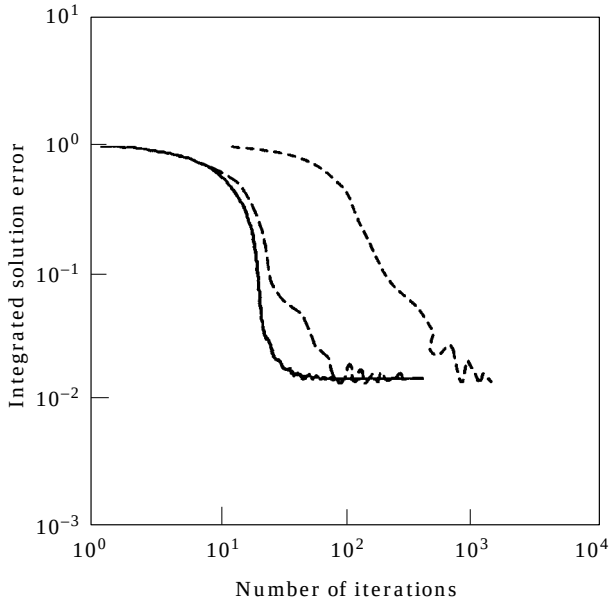

Figure 8. Integrated solution error as a function of the number of iterations of the finite difference equations ($f = 1$) with optimal parameters: – – –, parabolic $\alpha = 0$ and $\beta = 1{\cdot}0$ (Figure 3); ———, mixed $\alpha = 0{\cdot}95$ and $\beta = 1{\cdot}0$ (Figure 4); ——, optimum $\alpha = 1{\cdot}0$ and $\beta = 1{\cdot}01244$.

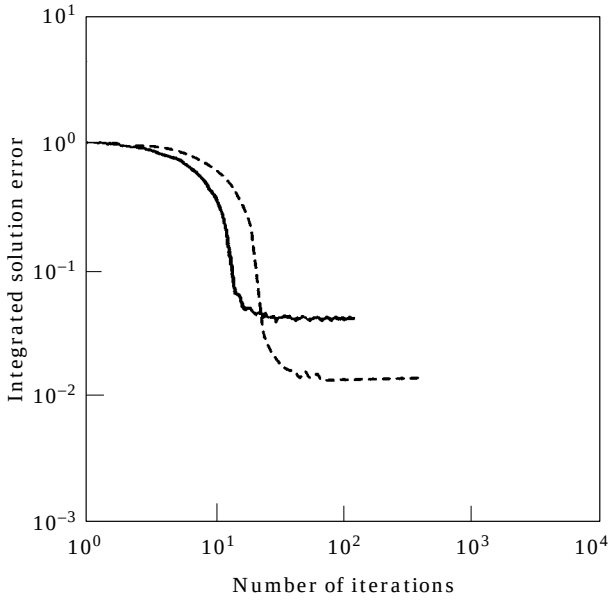

Figure 9. Integrated solution error as a function of the number of iterations of the finite difference equations ($f = 1$) with optimal parameters: – – –, $\Delta x = 0{\cdot}05$; ——, $\Delta x = 0{\cdot}083$.

The speed at which the transient solution approaches the steady state Helmholtz solution is now discussed.

10. SPEED OF PROPAGATION

With the preconditioned Helmholtz equation (9) and $\alpha = 1$, numerical experiments indicate that the steady-state solution $\psi(x)$ to the Helmholtz equation propagates outward at the dimensionless speed C, where from equation (2),

$$C = \frac{1}{f} = \frac{C_o^{\#}}{f^{\#} D^{\#}}. \tag{20}$$

For a frequency $f = 1$, Figure 12(a) shows the developing wave front (real and imaginary parts) as a function of the iteration number while Figure 12(b) shows the magnitude of the potential. For this case,

$$t = \frac{L}{C} = Lf = 1 \cdot 1 = 1. \tag{21}$$

As seen in Figure 12, the solution moves to the right with a distinct front at the speed $C = 1$. The front arrives at the exit at $t \approx 1{\cdot}0$.

Similarly, for a frequency $f = 5$, Figure 13(a) shows the developing wave front (real and imaginary parts) as a function of the iteration number while Figure 13(b) shows the magnitude of the potential. For this case,

$$t = \frac{L}{C} = Lf = 1 \cdot 5 = 5. \tag{22}$$

As seen in Figure 13, the solution moves to the right with a distinct front at the speed $C = 0{\cdot}2$. The front arrives at the exit at $t \approx 5{\cdot}0$.

The number of axial grid points and the number of iterations required for convergence are both directly proportional to frequency. A comparison of Figures 12 and 13 shows the factor of 5 difference in the number of required iterations when the frequency is increased by 5. For increased frequency, the solution moves more slowly to the right. For a duct of unit length, generally, the solution time should be increased by 30% over that predicted by equations (21) or (22) for more accurate results.

11. REFLECTION FREE TERMINATION

Extensive work exists in the literature in specifying a reflection free termination for wave propagation problems. Silvester and Pelosi [7] present a collection of 16 key papers which address the subject of reflection free absorbing boundary conditions. For their parabolic solution in the transient-frequency domain, Baumeister and Kreider [2] employed an impedance approximation for a reflection free termination in a finite length duct. However, an exact multimodal reflection free termination for a finite length duct can be achieved by a very simple artifice in the method developed in this paper.

As observed in Figure 13 for the $f = 5$ case, the steady-state Fourier transformed solution propagates outward with a well-defined front. Behind the front, the steady-state

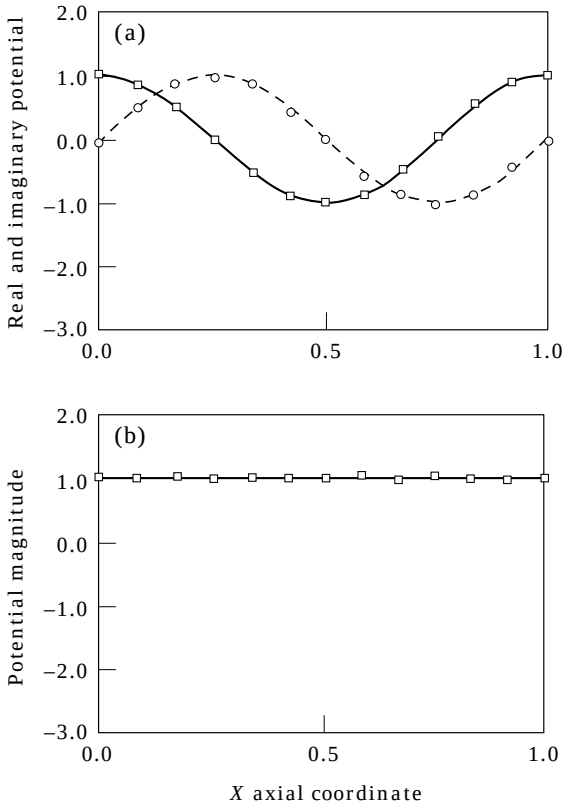

Figure 10. Analytical and numerical potential profile along wall for plane wave propagation in a semi-infinite hard walled duct ($f = 1$) with optimal parameters and $\Delta x = 0{\cdot}083$. (a) Real and imaginary parts. Numerical solution: □, real potential; ○, imaginary potential. Exact analytical solution: ——, real potential; – – –, imaginary potential. (b) Magnitude numerical solution: □, magnitude potential. Exact analytical solution: ——, magnitude.

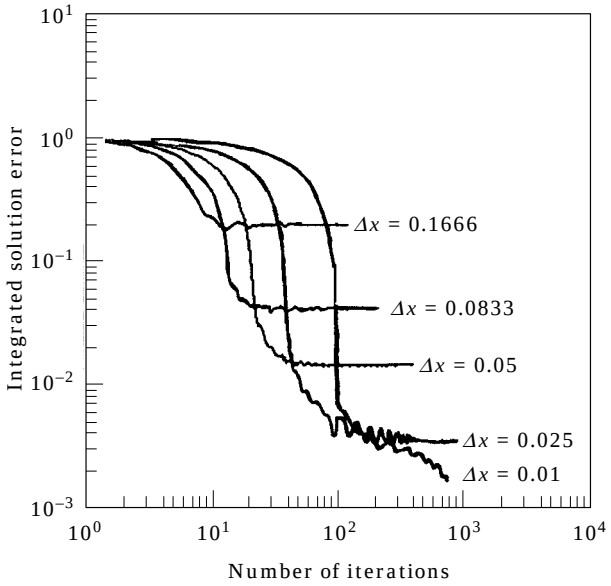

Figure 11. Integrated solution error as a function of grid spacings.

solution is fully developed. Ahead of the front, the potential remains zero. Thus, a reflection free termination for a duct can be accomplished by adding a small extension at the end of the duct, as shown in Figure 14. Once the wave front reaches the duct exit, the calculation time is extended to include the time for the wave front to reach the end of the extended region and reflect back to the end of the duct. This provides sufficient time for the steady-state solution to become fully developed in the duct. A large set of numerical experiments shows that an extension of 25% of the duct length is sufficient to provide accurate results. The length of the extension in Figure 14 can easily be increased or decreased to check for proper convergence.

As an example, consider the case of plane wave propagation at $f = 5$ in a unit length duct with a reflection free termination at $x = 1$. For this case, the time for the steady-state solution to reach the end of the duct is roughly $t = 5$ as calculated in equation (22) of section 10. With the added extension of $\Delta L = 0{\cdot}3$ shown in Figure 14, the time for a wave to propagate to the end of the extension and reflect back is estimated to be

$$t = \frac{\text{distance}}{\text{velocity}} = \frac{\Delta L}{C} = \Delta L f$$

$$= \underset{\text{forward}}{0{\cdot}3 * 5} + \underset{\text{reflected}}{0{\cdot}3 * 5} = 3. \tag{23}$$

Thus, the final solution shown in the bottom Figure 13(a) for $t = 8$ represents a reflection free termination at $x = 1$ by the simple addition of 0·3 length duct extension added to the end of the duct. Of course, the calculation must be stopped at $t = 8$. Longer solution times would allow reflections to enter back into the solution region and contaminate the reflection free termination. The exit boundary condition shown in Figure 14 can be rigid or absorbing, since its values will not affect the results in the duct.

The absorbing region should be lengthened or shortened to check for convergence. Advantageously, this approach is applicable to multimodal acoustic propagation, such as the soft-wall absorber case considered in the next section.

12. ATTENUATION OF A LINED SOFT-WALL ABSORBING DUCT

As the last example, consider the attenuation of a plane wave propagating through a lined soft-wall absorbing duct as shown in Figure 15. First, the relationship between the acoustic potential and energy propagation is established. This is followed by the development of the impedance concept in the transient frequency domain. Finally, a calculation for the attenuation is presented and compared to the exact analytical result computed by Rice [8].

The dimensionless time-averaged acoustic intensity I_x can be defined as

$$I_x = \frac{I_x^{\#}}{\rho_o^{\#} C_o^{\#3}} = \tfrac{1}{2}\Re(p_{ss}^{*}\phi_{x,ss}), \qquad \phi_{ss} = \lim_{t\to\infty}\phi,$$

$$P'(x, y, t) = p(x, y, t)\, e^{i2\pi t}, \qquad p_{ss} = \lim_{t\to\infty} p. \tag{24}$$

where p_{ss} and $\phi_{x,ss}$ represent the Fourier transformed steady-state value of the acoustic pressure and axial acoustic velocity. These values are determined at the completion of the transient analysis (subscript *ss* represents steady-state value). The * represents the complex

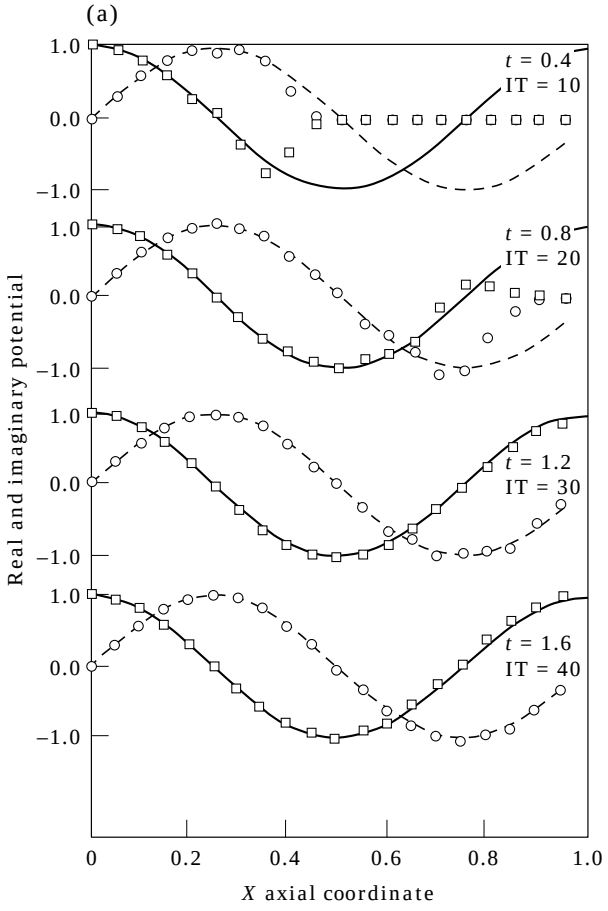

Fig.12(a)—(*caption on facing page*)

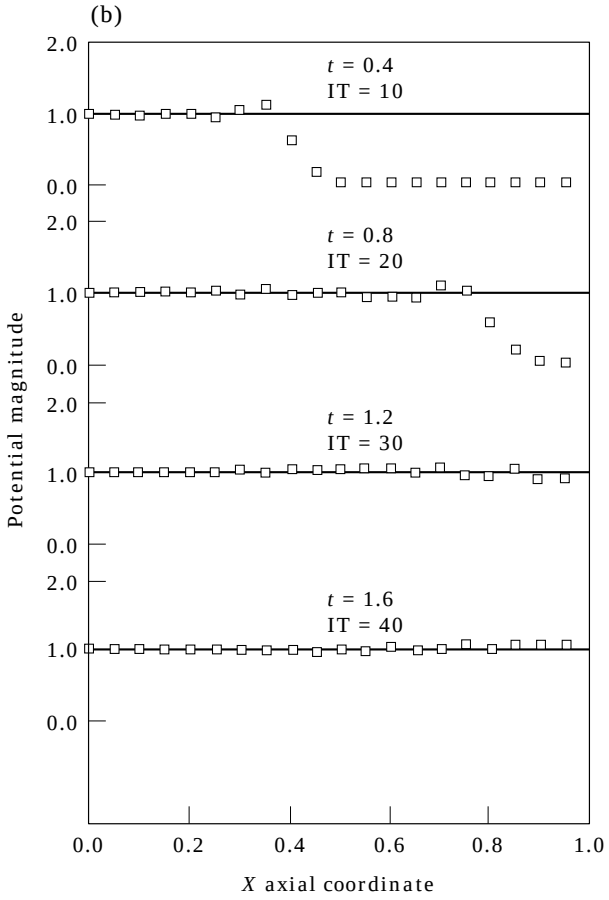

Figure 12. Developing history of disturbance propagation in Fourier transformed domain as a function of number of iterations (IT) and time ($f = 1$) with optimum parameters. (a) Real and imaginary parts. Numerical solution: □, real potential; ○, imaginary potential. Exact analytical solution: ——, real potential; – – –, imaginary potential. (b) Magnitude. Numerical solution: □, magnitude potential. Exact analytical solution: ——, magnitude.

conjugate of p_{ss}. The steady-state pressure is related to the potential by the relationship [2; combine equations (7) and (14) in reference [2] and set ϕ_t to zero]

$$p_{ss} = i\omega\bar{\rho}\phi_{ss}, \tag{25}$$

where $\bar{\rho}$ is the mean fluid density.

The total dimensionless acoustic power is the integral of the intensity across the duct section,

$$E_x = \int_0^1 I_x \, \mathrm{d}y. \tag{26}$$

By definition, the sound attenuation (the decrease in decibels of the acoustic power from $x = 0$ to $x = 1$) can be written as

$$\Delta \text{ dB} = 10 \log_{10} (E_1/E_0). \tag{27}$$

The values of acoustic intensity, axial power and attenuation can be calculated by the finite difference method in the transient-frequency domain. To perform these calculations, the wall impedance $Z^{\#}$ is introduced into the finite difference equations.

The soft-wall absorption is modelled by the impedance $Z^{\#}$, defined as [9, equation (34), section 15.4, p. 299]

$$Z^{\#} = \frac{P'^{\#}}{u_n'^{\#}} = \frac{P'^{\#}}{\nabla\phi'^{\#} \cdot n}, \tag{28}$$

where $P'^{\#}$ is the transient acoustic pressure and $u_n'^{\#}$ is the component of the acoustic particle velocity normal to its surface, pointing into the medium characterized by $Z^{\#}$. Here, n represents the unit outward normal. In dimensionless form, equation (28) for the wall impedance can be written as

$$\zeta = \frac{Z^{\#}}{\bar{\rho}^{\#} C_o^{\#}} = \frac{P'}{\phi_y'}. \tag{29}$$

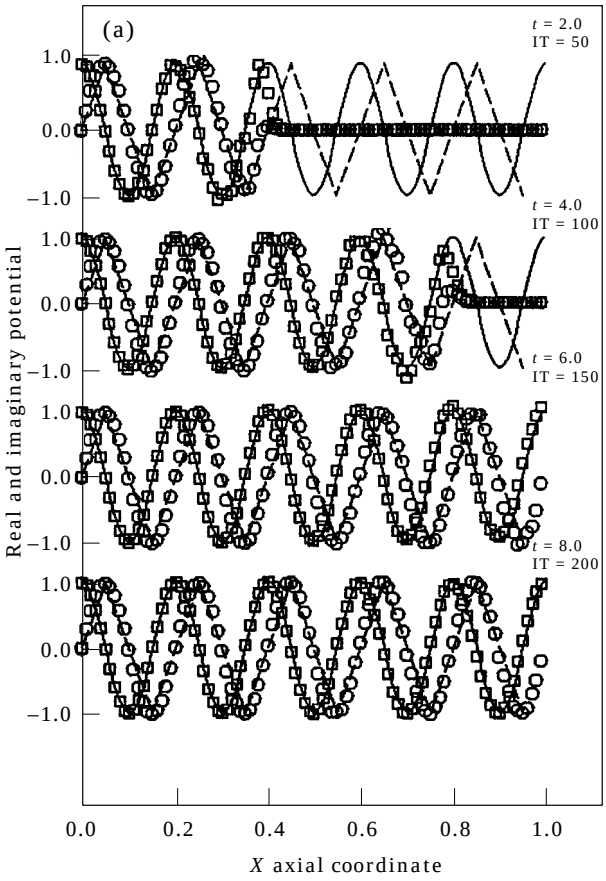

Fig. 13(a)—(*caption on facing page*)

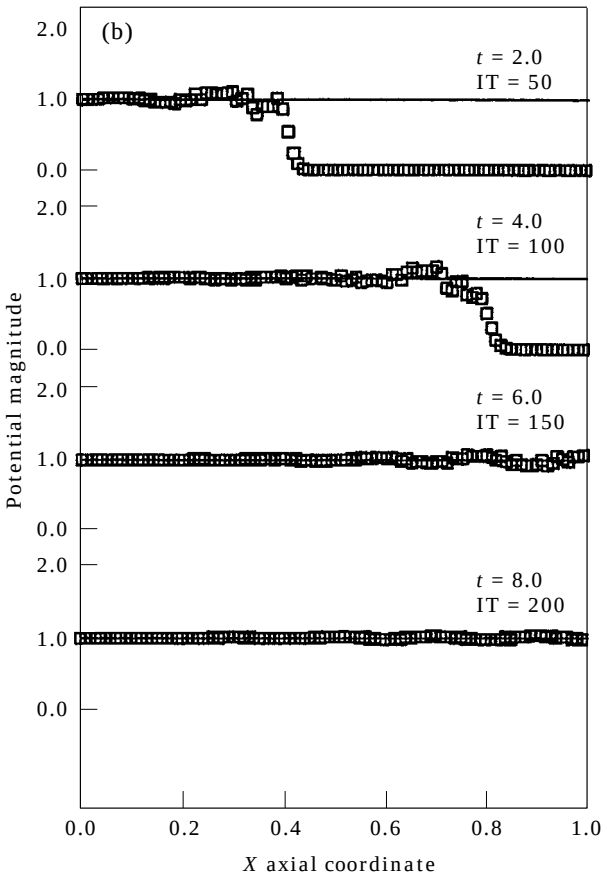

Figure 13. Developing history of disturbance propagation in Fourier transformed domain as a function of number of iterations (IT) and time ($f = 5$) with optimum parameters. (a) Real and imaginary parts. Numerical solution: □, real potential; ○, imaginary potential. Exact analytical solution: ——, real potential; – – –, imaginary potential. (b) Magnitude. Numerical solution: □, magnitude potential. Exact analytical solution: ——, magnitude.

The relationship between fluctuating acoustic pressure and potential is given by [2, equation (7)]

$$P' = -\bar{\rho} f \phi_i', \tag{30}$$

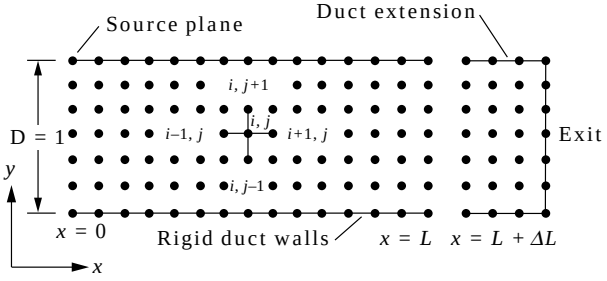

Figure 14. Duct extension to simulate reflection free exit condition.

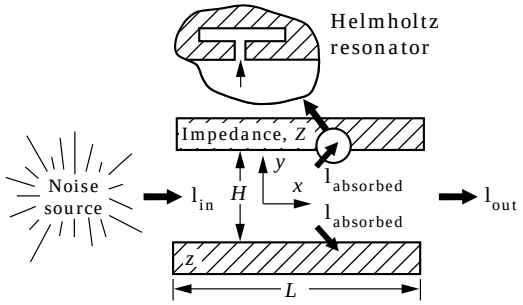

Figure 15. Schematic of suppressor duct using a Helmholtz resonator.

which can now be substituted into equation (29) to yield the soft-wall gradient condition of the potential at the wall,

$$\phi'_y = \frac{-\bar{\rho} f \phi'_t}{\zeta} . \tag{31}$$

Equation (31) must now be expressed in terms of the transient-frequency domain variable ϕ to perform the difference analysis. Employing the transformation given by equation (6) yields for the gradient at the wall

$$\phi_y = \frac{+\bar{\rho} i\omega\phi}{\zeta} - \frac{\bar{\rho} f \phi_t}{\zeta} . \tag{32}$$

Thus, in the transient-frequency domain, the soft-wall gradient has a transient component of the potential coupled to the wall impedance. After sufficient time, the transient term in equation (32) decays to zero. However, this transient contribution is required in developing a stable soft-wall difference formulation. Neglecting this term leads to an unstable finite difference formulation. As before, the procedure for developing the soft-wall finite difference equation is given in detail by Baumeister [4].

Now consider the duct displayed in Figure 14 with dimensionless height $H = 1$, dimensionless length $L = 1$ and dimensionless frequency $f = 1$. A reflection free termination condition is assumed to exist at the duct exit $x = 1$. The grid spacing is set at $\Delta x = 0{\cdot}05$ and $\Delta y = 0{\cdot}1$. For this frequency and duct length, the wall impedance is assumed to have the optimum value of wall impedance (maximum attenuation) of

$$\zeta = 0{\cdot}46 + i0{\cdot}92. \tag{33}$$

Because the stable time increment from equation (18) was 0·045, a conservative time increment of 0·04 is used in the calculation.

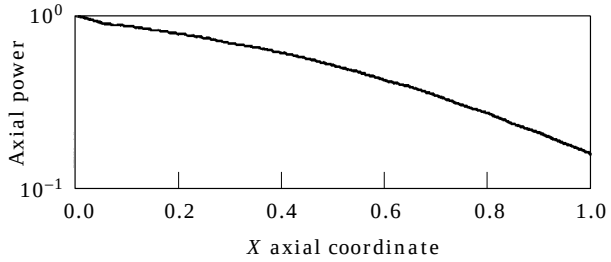

Figure 16. Axial power as a function of position in the duct ($f = 1$).

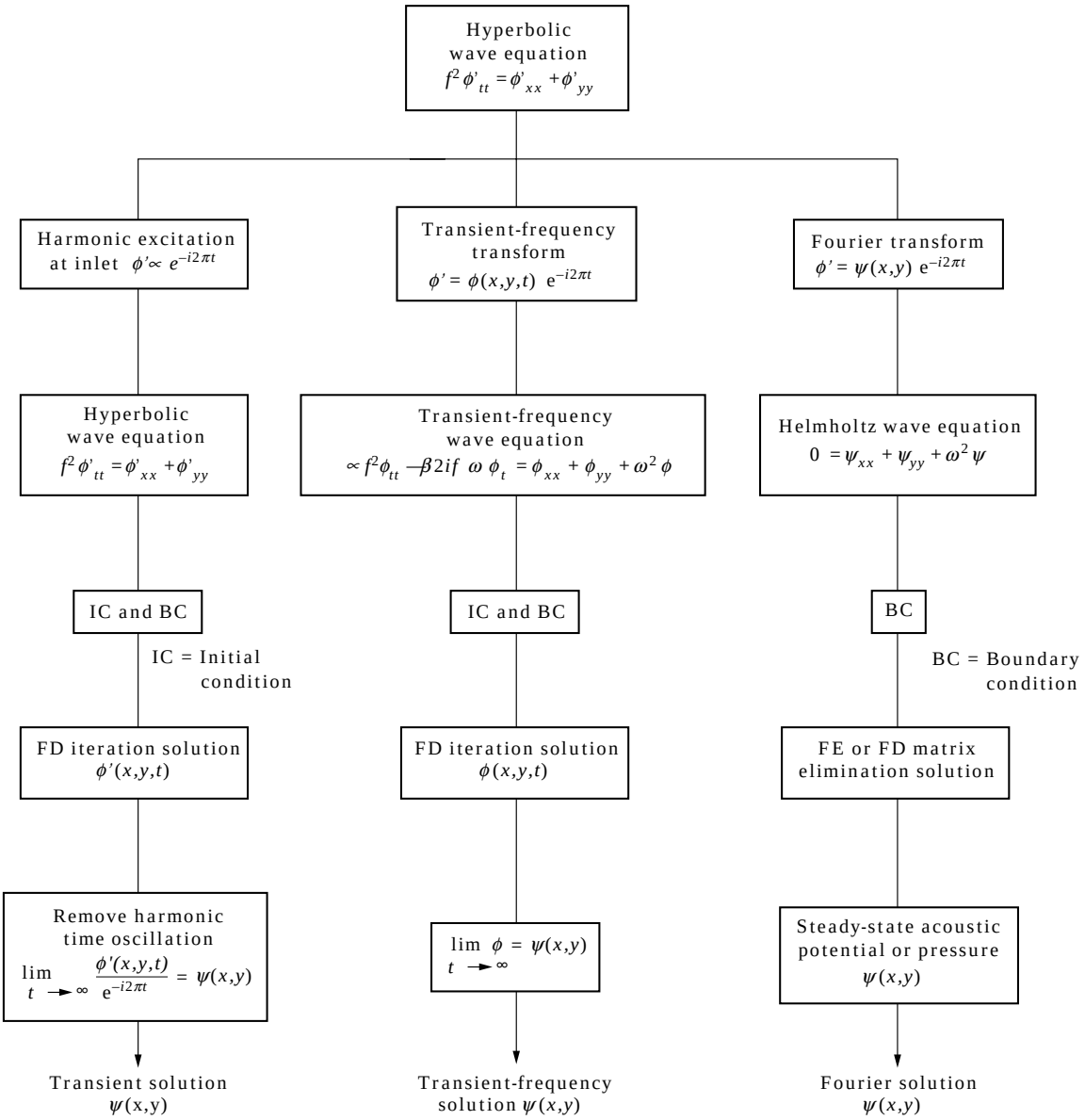

Figure 17. Alternate finite difference/element methods in solving wave equations.

The calculated power as a function of axial position is shown in Figure 16. The decrease in axial power is due to the absorption of the wall represented by the impedance ζ. The attenuation as calculated by equation (27) is 8·1 dB, which compares favorably to the exact analytical value of 8·2 dB as calculated by Rice [8].

13. SOLUTION METHODS

With the approach developed in this paper, three different finite difference of finite element solution techniques are now available to solve the Helmholtz equation, as shown in Figure 17.

The Fourier transform approach in the right column, with finite differences or finite elements, results in a matrix equation. Because this matrix is not positive definite, matrix elimination solutions are generally employed, requiring extensive computer memory for high frequency propagation. The transient solution to the hyperbolic wave equation, shown in the left column, eliminates matrix storage requirements by iterating finite difference approximations to the steady state solution.

The third option, hyperbolic preconditioning using the mixed formulation ($\alpha \neq 0$, $\beta \neq 0$), is shown in the center column. This approach eliminates matrix storage requirements, and has less stringent stability conditions than the transient solution, so it converges in fewer iterations.

14. CONCLUSION

Accelerated numerical preconditioning of the Helmholtz equation has been developed. The field is iterated in time from an initial value of 0 to attain the steady-state solution. The method eliminates the large matrix storage requirements of steady-state finite difference or finite element techniques in the frequency domain. In each example provided, the numerical solution quickly and accurately converges to the exact steady-state solution. The hyperbolic preconditioning developed in this paper has more than an order of magnitude faster convergence than the previously developed parabolic preconditioning approach.

ACKNOWLEDGMENT

The bulk of this research was done at the NASA Lewis Research Center before the retirement of the first author. We would like to thank NASA's John Abbott and Lou Povinelli for their support in this research.

REFERENCES

1. A. Bayliss, C. I. Goldstein and E. Turkel 1983 *Journal of Computational Physics* **49**, 443–457. An iterative method for the Helmholtz equation.
2. K. J. Baumeister and K. L. Kreider 1996 *ASME Journal of Vibration and Acoustics* **118**, 622–629. Finite difference time marching in the frequency domain: a parabolic formulation for the convective wave equation.
3. E. Turkel and A. Arnone 1993 *Proceedings of the* 11*th AIAA Computational Fluid Dynamics Conference*, 349–357, *AIAA Paper* 93-3329. Pseudo-compressibility methods for the incompressible flow equations.
4. K. J. Baumeister 1980 *AIAA Journal* **18**, 1470–1476. Time-dependent difference theory for noise propagation in a two-dimensional duct.
5. K. J. Baumeister 1982 *ASME Journal of Engineering for Industry* **104**, 113–120. Influence of exit impedance on finite-difference solutions of transient acoustic mode propagation in ducts.
6. A. Cabelli 1982 *Journal of Sound and Vibration* **85**, 423–434. Duct acoustics—a time dependent difference approach for steady state solutions.
7. P. P. Silvester and G. Pelosi 1994 *Finite Element for Wave Electromagnetics*, *Methods and Techniques*. IEEE Press.
8. E. J. Rice 1968 *Aerodynamic Noise Proceedings of the AFOSR-UT/AS Symposium* (H. S. Ribner, editor) *University of Toronto*, *Canada*, 229–250. Attenuation of sound in soft-walled circular ducts.
9. E. Skudrzyk 1971 *The Foundations of Acoustics*. New York: Springer-Verlag.

APPENDIX: NOMENCLATURE

$C_o^\#$	dimensional speed of sound
C	dimensionless speed of sound
$D^\#$	dimensional duct height
D	duct height, $D^\#/D_o^\#$, $D = 1$
E_x	acoustic power in x direction
e_k	total L_1 convergence error at step k
$e_{k\lambda}$	e_k error per axial wavelength
$f^\#$	dimensional frequency
f	dimensionless frequency, $f^\# D^\#/C_o^\#$
I_x	dimensionless intensity in x direction
i	$\sqrt{-1}$
L	length of duct, $L^\#/D^\#$
$\|M\|$	absolute value of Mach number
n	unit outward normal
P'	transient dimensionless acoustic pressure, $P'^\#/\rho_o^\# C_o^{\#2}$
p	transient dimensionless acoustic pressure in frequency space
t	dimensionless time, $f^\# t^\#$
t_T	dimensionless total calculation time
Δt	time step
u_n	normal acoustic particle velocity
x	dimensionless axial coordinate, $x^\#/D^\#$
Δx	axial grid spacing
y	dimensionless transverse coordinate, $y^\#/D^\#$
Δy	transverse grid spacing
$Z^\#$	impedance
α	acceleration parameter
β	acceleration parameter
Δ dB	decrease in decibels
ζ	dimensionless impedance, $Z^\#/\rho_o^\# C_o^\#$
$\bar{\rho}$	mean steady fluid density
ψ	Fourier transformed potential
ω	dimensionless frequency, $2\pi f$

Subscripts

i	axial index, see Figure 1
j	transverse index, see Figure 1
o	ambient or reference condition
ss	steady-state Fourier transform values

Superscripts

#	dimensional quantity
k	time step
*	complex conjugate